

Article

Hydrothermal Investigation of a Microchannel Heat Sink Using Secondary Flows in Trapezoidal and Parallel Orientations

Safi Ahmed Memon ¹, Taqi Ahmad Cheema ^{2,*}, Gyu Man Kim ¹ and Cheol Woo Park ^{1,*}

¹ School of Mechanical Engineering, Kyungpook National University, 80 Daehakro, Buk-gu, Daegu 41566, Korea; safibta@gmail.com (S.A.M.); gyuman.kim@knu.ac.kr (G.M.K.)

² Faculty of Mechanical Engineering, Ghulam Ishaq Khan Institute of Engineering Sciences & Technology, Topi 23460, Pakistan

* Correspondence: tacheema@giki.edu.pk (T.A.C.); chwoopark@knu.ac.kr (C.W.P.); Tel.: +92-938-271858 (T.A.C.); +82-53-950-7569 (C.W.P.)

Received: 14 September 2020; Accepted: 22 October 2020; Published: 27 October 2020



Abstract: Thermal performance enhancement in microchannel heat sinks has recently become a challenge due to advancements in modern microelectronics, which demand compatibility with heat sinks able to dissipate ever-increasing amounts of heat. Recent advancements in manufacturing techniques, such as additive manufacturing, have made the modification of the microchannel heat sink geometry possible well beyond the conventional rectangular model to improve the cooling capacity of these devices. One such modification in microchannel geometry includes the introduction of secondary flow channels in the walls between adjacent mainstream microchannels. The present study computationally models secondary flow channels in regular trapezoidal and parallel orientations for fluid circulation through the microchannel walls in a heat sink design. The heat sink is made of silicon wafer, and water is used as the circulating fluid in this study. Continuity, momentum, and energy equations are solved for the fluid flow through the regular trapezoidal secondary flow and parallel secondary flow designs in the heat sink with I-type, C-type, and Z-type inlet–outlet configurations. Plots of velocity contours show that I-type geometry creates optimal flow disruption in the heat sink. Therefore, for this design, the pressure drop and base plate temperatures are plotted for a volumetric flow rate range, and corresponding contour plots are obtained. The results are compared with corresponding trends for the conventional rectangular microchannel design, and associated trends are explained. The study suggests that the flow phenomena such as flow impingement onto the microchannel walls and formation of vortices inside the secondary flow passages coupled with an increase in heat transfer area due to secondary flow passages may significantly improve the heat sink performance.

Keywords: thermal performance; microchannels; secondary flow; flow disruption

1. Introduction

Miniaturisation of modern microelectronic components coupled with a continual increase in their heat dissipation has fuelled the demand for advanced heat sinks at the microscale. Tuckerman and Pease first introduced the concept of microchannels with internal convection as electronic cooling devices [1]. These devices, also known as microchannel heat sinks (MCHS), need to be capable of cooling microelectronic chips dissipating heat on the order of 10^5 W/cm³ to meet modern-day demand [2]. With its prominent heat transfer characteristics, such as a high surface-area-to-volume ratio, high heat transfer coefficients, low thermal resistance, and high order of compactness, the device has gained considerable attention from researchers in the thermal management community. Commercially,

electronic chip cooling devices generally use MCHS with straight rectangular cross-section channels due to its simple design, convenient integration and easy manufacturing methods, with a reasonable increase in heat transfer [3]. However, maintaining safe operating temperatures in the rectangular MCHS design is becoming increasingly difficult due to the high thermal dissipation of the modern electronic chips [4]. Two key ways to solve this impending concern include increasing the heat transfer area with passive techniques and enhancing the coolant's thermophysical properties [5].

Researchers in the past few decades worked to enhance the thermal characteristics of the MCHS designs by employing various techniques such as altering the channel geometry, introducing different working fluids, and changing the flow behaviour [6–15]. Many employed experimental methods to enhance thermal characteristics, such as Reyes et al., who experimentally studied thermal enhancement and pressure drop in conventional MCHS with tip clearance and compared the results with those of a reference geometry having conventional rectangular characteristics [6]. However, owing to the high cost of experimental investigation, researchers are employing computational methods to analyse flow in various configurations in MCHS. For instance, Hung et al. developed three-dimensional models of MCHS, optimising the geometry to reduce the total thermal resistance of the device, for differently layered geometrical configurations [7]. Various geometric parameters, such as channel count, width, aspect ratio, and tapered ratios, were varied in their study. Hung and Yan tested various parameters that might affect the heat absorption and found the thermal resistance to be more sensitive to the number of channels, channel width, and width-tapered ratio, and less sensitive to the height-tapered ratio of the microchannel [8]. The authors further concluded that higher pumping power resulted in a greater decrease in thermal resistance. Akbar et al. computationally studied the thermal performance in a truncated double-layered heat sink design [9]. The authors observed that a decrease in the dimensionless values of truncated lengths resulted in a decrease in thermal resistance and temperature deviation at the bottom wall of the microchannels.

Increasing flow disruptions, decreasing the thermal boundary layer, or increasing the velocity gradient near the heat sink wall are efficient ways to improve the thermal management ability of a heat sink, as suggested by Tao et al. [10]. To introduce these flow disruption phenomena, Steinke and Kandlikar further recommended optimising the geometry of the microchannels to minimise the negative impacts on flow properties and suggested fabricating microchannel geometries that promote fluid mixing in the channels [11]. Following the suggestions of Steinke and Kandlikar, Raja et al. studied the disruption in the hydrodynamic boundary layer due to fluid flow through slanted passages in the microchannel walls between adjacent channels [12]. The flow mechanism with secondary flow passages enhanced the thermal performance with a minor pressure drop. Lu and Wang strategically varied the placement of inlet and outlet locations in a heat sink design to characterise the flow disruption and associated heat transfer enhancement [13]. Their study suggested that strategic placement of the inlet and outlet in a heat sink for optimal thermal absorption can significantly improve its performance. Brinda et al. proposed a ladder-shaped microchannel with two parallel rectangular channels connected with one or more link channels [14]. The authors concluded that large disturbances in the flow, fluid mixing, and change in flow direction contribute to enhanced heat transfer. Leela et al. tested four different heat sink geometries, each consisting of four different microchannels with separate inlets and outlets [15]. The authors observed several regions of developing flow. A higher heat transfer rate than conventional microchannel geometry was observed in their study. More recently, Rehman et al. evaluated the thermal and hydrodynamic performance of a heat sink with hydrofoil-shaped sidewall rib-employed microchannels [16]. They revealed that the size and fabrication of a microchannel heat sink limit the heat transfer by hydrofoil shaped ribs in MCHS. The authors also concluded that a disparity in rib extents and coolant properties can increase the thermal performance of microchannels. Ahmad et al. analysed MCHS with cylindrical ribs and cavities [17]. They computationally investigated the effect of different design configurations of cylindrical ribs and cavities on the thermal and hydrodynamic performance of MCHS. Their results suggested that factors related to both the first and second laws of thermodynamics must be taken into account to

calculate the overall performance of the heat sinks. Xia et al. tested the use of different microchannel geometries for flow disruption in a heat sink design with fluid entering and exiting the heat sink normally through the header region to facilitate an even flow distribution into the microchannel cavities [18]. Two different designs of microchannels were computationally studied using the entire heat sink as the computational domain. Their study suggested that the interaction of fluid branching and friction of the walls of the header contributes to the improved flow mechanism. Furthermore, they described jetting and throttling behaviour of flow near the channel and the drag due to the re-entrant cavities as contributors to heat transfer. However, in their study, hotspots were obtained on the base plate of the heat sink in the vicinity of the microchannels near the outlet of the heat sink.

The present study considers the heat sink design studied by [18], in which the fluid enters the heat sink normally through the header region and is distributed evenly into microchannel cavities. Rectangular microchannels with secondary flow passages between adjacent mainstream microchannels in regular trapezoidal and parallel orientations are incorporated in the heat sink design. Different inlet–outlet configurations are tested for optimal flow distribution inside the heat sink and hydrothermal effects of the secondary flow in terms of pressure and velocity profiles in the fluid domain, and temperature profiles on the base plate are studied. Velocity and pressure contour plots obtained in the present study, suggest the existence of flow impingement into microchannel walls, vortex generation inside the secondary flow channels, and the Coanda effect on the lateral walls of the heat sink, which contribute to the overall thermal performance of the heat sink. Temperature contour plots on the base plate suggest that the improved design better eliminates hotspots in the vicinity of the microchannels compared to the previous design in the literature.

2. Methodology

2.1. Model Description

In the present study, the effects of two different microchannel designs with secondary flow passages are studied in a heat sink model. Figure 1a shows the sectional view of the heat sink geometry under consideration. The coolant enters normally through the inlet in the header region and spreads into the microchannel cavities, where it absorbs a heat flux from the microelectronic source mounted on the base plate. The fluid leaves normally through the outlet in the header region at the opposite end. The walls of the microchannels consist of secondary flow passages, which facilitate the intermixing of the coolant between the adjacent channels. The two different designs for the secondary flow considered in this study are the secondary flow channels in regular trapezoidal and parallel orientations, as shown in Figure 1b,c, and the corresponding heat sinks are referred to in this paper as heat sinks A and B, respectively. The heat sinks are made of silicon, and water is used as the coolant for this study. The two microchannel designs are tested against the three inlet–outlet configurations—I-type, C-type and Z-type—in the heat sink, as depicted in Figure 2. The configuration with optimal flow distribution is identified for each microchannel design, and the pressure, velocity and temperature profiles are analysed for the heat flux of 1.2×10^6 W/m² and the volumetric flow rate range of 2.0×10^{-6} m³/s to 4.0×10^{-6} m³/s.

The geometric configuration of the heat sink under study is shown in Figure 3. The mainstream channels in the heat sinks have a hydraulic diameter (D_h) of 1.5×10^{-4} m. The number of mainstream channels (n_{ch}) is 30 in each heat sink considered, and the number of secondary flow passages in each wall between the channels is 10 over the length of the microchannels in heat sinks A and B. Various parameters of the heat sink are presented in Table 1. Figure 4a,b shows the geometric configuration of the regular trapezoidal and parallel secondary flow passages. The expressions and values of associated parameters are given in Table 2.

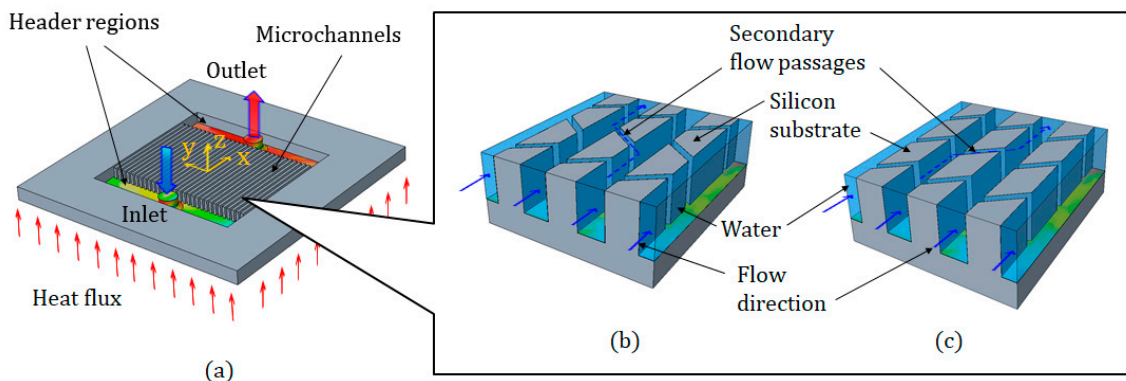


Figure 1. (a) Sectional view of the microchannel heat sink; (b) close-up view of the regular trapezoidal secondary flow (heat sink A); (c) close-up view of the parallel secondary flow (heat sink B).

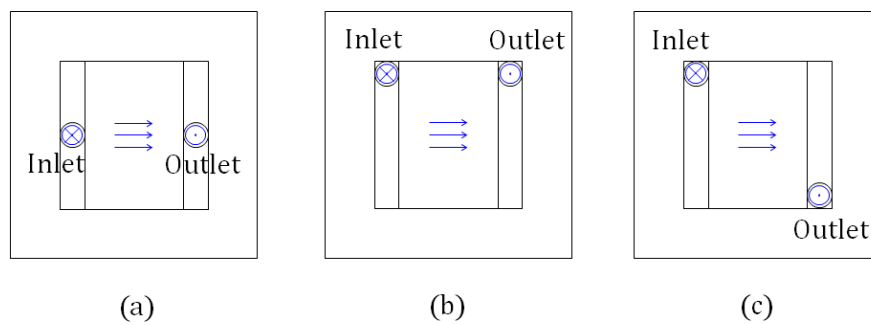


Figure 2. Different inlet–outlet configurations for flow disruption study: (a) I-type configuration, (b) C-type configuration, and (c) Z-type inlet–outlet configuration.

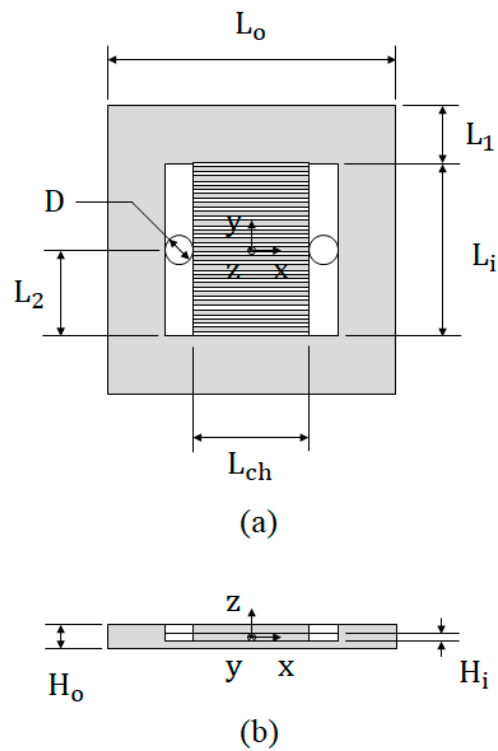


Figure 3. Geometric configuration of the I-type microchannel heat sink: (a) top view and (b) side view.

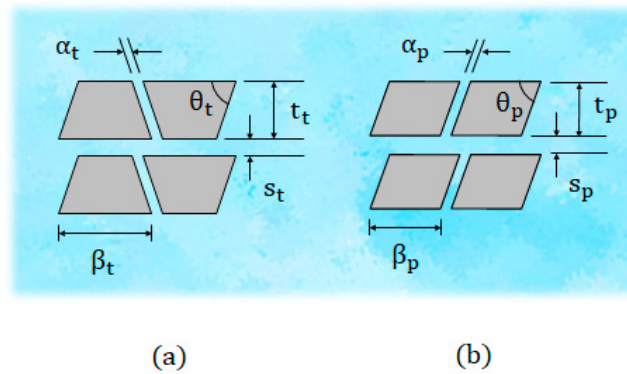


Figure 4. Detailed view of the microchannel walls with (a) regular trapezoidal secondary flow passages and (b) parallel secondary flow passages.

Table 1. Geometric configuration of the heat sinks.

Dimension	Value ($\times 10^{-3}\text{m}$)
L_o	10.0
L_i	6.0
H_o	9.0
H_i	0.3
D	1.0
D_h	0.15
L_{ch}	4.0
$L_1 = (L_o - L_i)/2$	2.0
$L_2 = L_i/2$	3.0

Table 2. Geometric configuration of the microchannels.

Microchannel Design	Parameters				
	α_ξ (m)	s_ξ (m)	θ_ξ (deg)	β_ξ (m)	t_ξ (m)
Heat sink A	1.0×10^{-4}	1.0×10^{-4}	45	4.0×10^{-4}	$(L_i - n_{ch} \times s_\xi) / (n_{ch} - 1)$
Heat sink B	1.0×10^{-4}	1.0×10^{-4}	45	$\beta_t - (t_p / \tan \theta_\xi)$	$(L_i - n_{ch} \times s_\xi) / (n_{ch} - 1)$
$\xi = \begin{cases} t \text{ for regular trapezoidal secondary flow passages (heat sink A)} \\ p \text{ for parallel secondary flow passages (heat sink B)} \end{cases}$					
n_{ch} represents the number of microchannels in each heat sink ($n_{ch} = 30$)					

2.2. Governing Equations

A three-dimensional solid–fluid heat transfer conjugation model is used to solve the hydrodynamics of the heat sink. The following assumptions are considered to develop the heat transfer and fluid flow model associated with the working fluid and heat sink:

- i. The flow of water through the heat sink is assumed laminar and incompressible, and the study is conducted at steady state.
- ii. The flow obeys continuum theory with Navier–Stokes equations applicable in the fluid domain.
- iii. The hydraulic diameter in this model is adequately large at microscale with a low Reynolds number so that the effects of viscous dissipation on energy equation can be neglected. [19]
- iv. Fluid and thermal slips at the solid–fluid interface inside the heat sink are neglected.
- v. The Peclet number for the flow has been assumed high enough for the heat transferred by conduction through the microchannel walls (i.e., axial conduction) to be neglected [20].
- vi. Heat transfer outward from the heat sink through convective or radioactive means is neglected.
- vii. Body forces such as gravitational force are neglected.

Given the above assumptions, the flow in the MCHS is governed by the following equations:

a. Continuity equation

$$\nabla \cdot \vec{u} = 0, \quad (1)$$

where \vec{u} represents the velocity field in the fluid domain.

b. Momentum equation

$$\nabla \cdot (\rho_f \vec{u} \vec{u}) = -\nabla p + \nabla \cdot (\mu_f \nabla \vec{u}), \quad (2)$$

where p is the fluid pressure; ρ_f and μ_f are the fluid density and dynamic viscosity of the fluid, respectively, and are assumed constant for this model.

c. Energy equation

$$\nabla \cdot (\rho_f \vec{u} c T_f) = \nabla \cdot (k_f \nabla T_f) \quad (\text{liquid}) \quad (3)$$

$$\nabla \cdot (k_s \nabla T_s) = 0 \quad (\text{solid}) \quad (4)$$

where T_f and T_s are the temperature fields inside the fluid and solid domains, respectively; c is the specific heat; c_f is the fluid specific heat; k_f and k_s are the thermal conductivities of the fluid and solid, respectively.

Boundary Conditions

In this simulation, the coolant flows into the heat sink at a constant inlet velocity and temperature. Atmospheric pressure has been set at the outlet along with convective outflow boundary condition. A uniform heat source exists at the base plate of the heat sink, while the remaining exterior walls of the heat sink are considered adiabatic. Temperature and heat flux are assumed continuous at the solid–fluid interface. Hence, the following boundary conditions are applied to the model:

a. Inlet

$$T_f = T_{in} = 293 \text{ K} \quad (5)$$

$$\mathbf{u} = \mathbf{u}_{in} \quad (6)$$

b. Outlet

$$p = p_{out} = 1 \text{ atm} \quad (7)$$

c. Fluid–solid interface:

$$\mathbf{u} = 0 \quad (8)$$

$$T = T_s \quad (9)$$

$$-k_s \left(\frac{\partial T_s}{\partial n} \right) = -k_f \left(\frac{\partial T_f}{\partial n} \right) \quad (10)$$

d. Base plate:

$$q_w = 1.2 \times 10^6 \text{ W/m}^2 \quad (11)$$

In the above equations, T_{in} and u_{in} are the temperature and velocity at the inlet of the heat sink, respectively; p_{out} is the pressure at the outlet; q_w is the heat flux at the base plate.

3. Numerical Method

A mixed grid composed of structured and unstructured elements has been used to discretise the governing equations. The elements are locally refined to capture flow properties perpendicular to the fluid–solid interface. Pressure and velocity are coupled using the segregated approach and the governing equations have been solved using PARDISO solver for the heat transfer and fluid flow variables.

3.1. Grid Independence Study

A grid independence study is conducted for the conventional heat sink model. Grids with 6.6×10^4 , 9.1×10^4 , and 2.0×10^5 elements are used, keeping the available computational resource in mind. Average base plate temperature is obtained for the volumetric flow rate of $3.0 \times 10^{-6} \text{ m}^3/\text{s}$ and absolute percentage difference of -0.34% and 0.16% is observed between the successive grids as shown in Table 3. To minimise the computational cost, the grid with 9.1×10^4 elements is used for the conventional model for further study. Consequently, the number of elements is kept at 2.6×10^5 for each of the heat sinks A and B.

Table 3. Grid independence study.

Number of Elements	Average Base Plate Temperature, $T_{b,ave}$ (k)	Percentage Difference
6.6×10^4	315.02	-
9.1×10^4	313.96	-0.34%
2.0×10^5	314.46	0.16%

3.2. Model Validation

The numerical model for the heat sink design with conventional microchannel design has been validated against the conventional model of Xia et al. [18] for the base plate temperature in the volumetric flow rate range of $1.33 \times 10^{-6} \text{ m}^3/\text{s}$ to $3.33 \times 10^{-6} \text{ m}^3/\text{s}$ and the base plate heat flux of $2.0 \times 10^6 \text{ W/m}^2$, as shown in Figure 5. With the available computation power and the selected grid, a maximum percentage error of 7.80% is observed for the model.

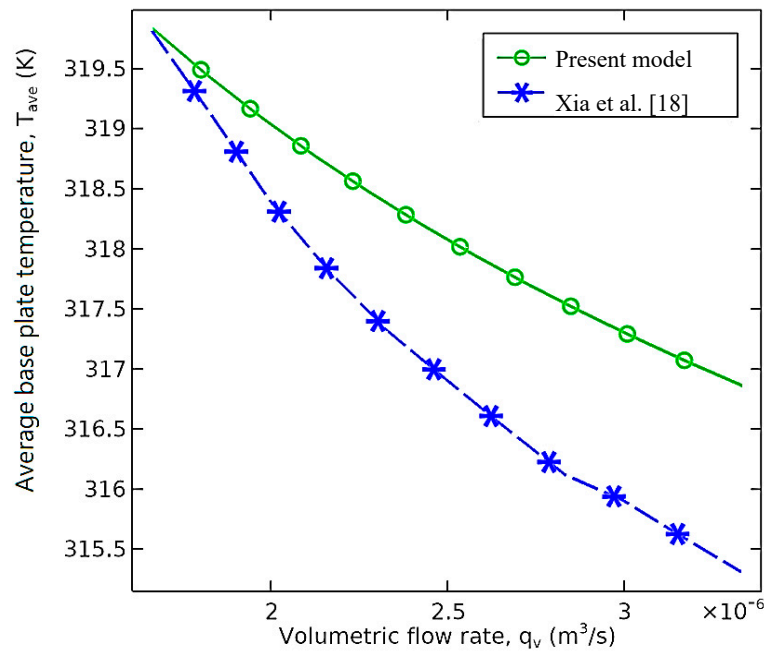


Figure 5. Comparison of base plate temperature with Xia et al. [18] for the heat flux of $2.0 \times 10^6 \text{ W/m}^2$.

4. Results and Discussion

4.1. Flow Distribution for Different Inlet–Outlet Configurations

The flow distribution is studied for the regular trapezoidal and parallel secondary flow designs of the heat sink with I-type, C-type, and Z-type inlet–outlet configurations to identify the configuration with optimal flow disruption for each of the microchannel designs. The volumetric flow rate of $4.0 \times 10^{-6} \text{ m}^3/\text{s}$ is used to analyse the flow disruption inside the heat sinks, and the velocity magnitude contours are plotted over the midplane ($z = 0$), as shown in Figure 6.

A certain degree of flow separation is observed inside the header regions for each of the three inlet–outlet configurations. For the inlet header regions, the higher flow velocity can be attributed to the normal flow of the fluid as it impinges onto the bottom surface of the heat sink before distributing into the microchannel cavities. Similarly, a higher velocity region at the outlet header can be explained as the fluid is collected from the microchannel cavities into the header region before exiting the heat sink. The flow separation near the outlet region is relatively lesser than the flow separation in the inlet header region. This phenomenon is due to the pressure drop that occurs in the microchannel region thereby resulting in lesser difference in pressure between the outlet header region and the outlet.

Additional fluid separation can be observed near the outward edges of the mainstream channels at the extreme ends of the heat sink. As the water from the fluid impinges onto the bottom surface and spreads in the direction of the microchannel cavities, the further end of the extreme microchannels becomes coated by a hydrophilic layer, causing the liquid to slip in that region. This effect is known as the Coanda effect, which can be easily explained by the use of the continuity equation of an incompressible fluid. Assuming planar flow in this region, Equation (1) suggests that the bending of the fluid in the positive x-direction will occur if the component of velocity in the y-direction decreases. The Coanda effect is more pronounced in the C-type and Z-type inlet–outlet configurations, where the inlets and outlets are located near the lateral walls of the heat sink, thereby resulting in increased velocity in the extreme channels. The effect is depicted in Figure 7, which shows the streamlines over the midplane ($z = 0$) of the heat sink with Z-type configuration in the vicinity of $x = -2.0 \times 10^{-3} \text{ m}$ and $y = 2.65 \times 10^{-3} \text{ m}$ at $4.0 \times 10^{-6} \text{ m}^3/\text{s}$ volumetric flow rate.

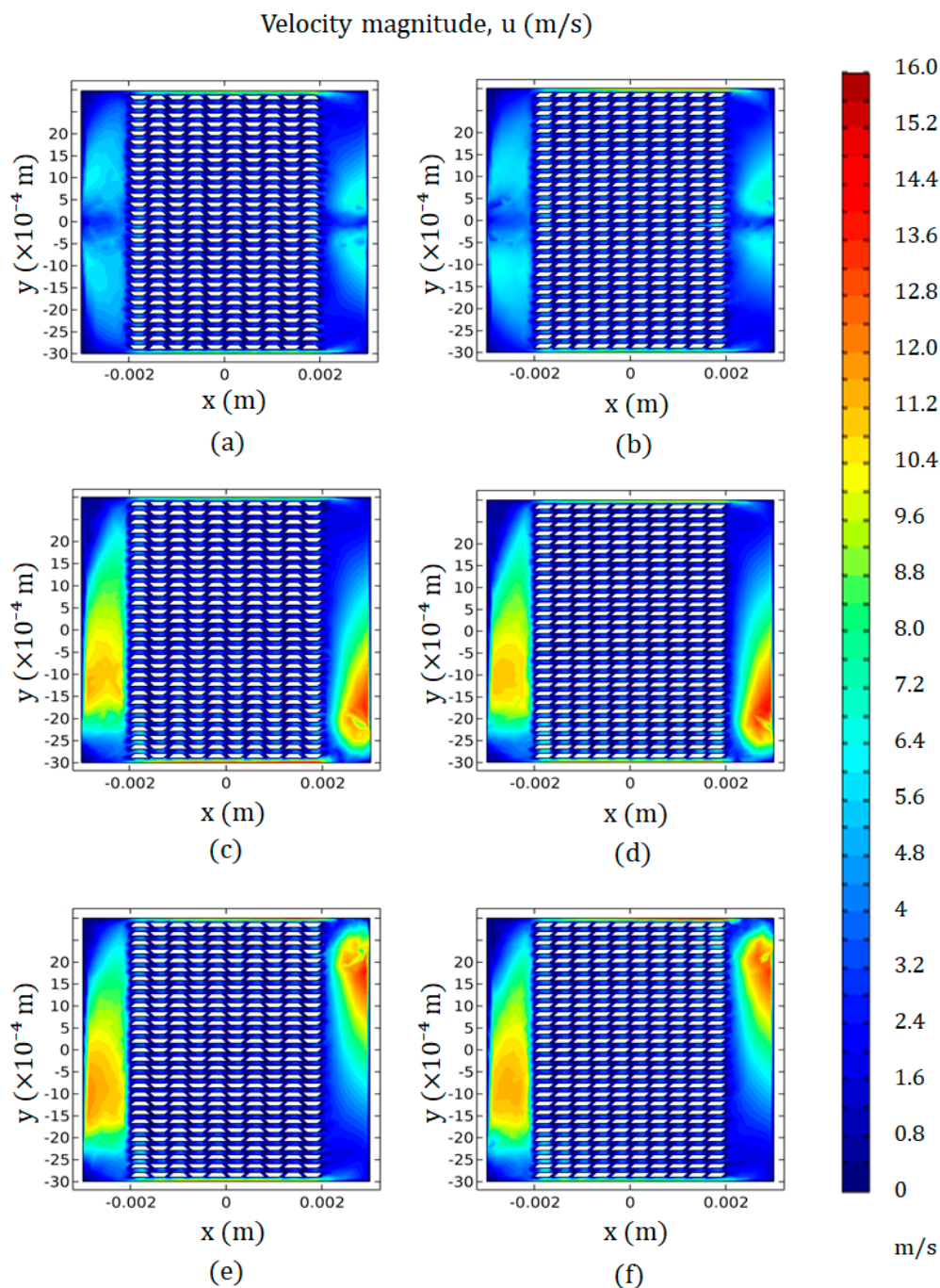


Figure 6. Contour plot of velocity magnitude at midplane ($z = 0$) of the heat sink at the volumetric flow rate of $4.0 \times 10^{-6} \text{ m}^3/\text{s}$ for the (a) I-type regular trapezoidal secondary flow, (b) I-type parallel secondary flow, (c) C-type regular trapezoidal secondary flow, (d) C-type parallel secondary flow, (e) Z-type regular trapezoidal secondary flow, and (f) Z-type parallel secondary flow.

The flow is uniform and fairly symmetric about the $y = 0$ planes in the I-type inlet–outlet configuration for both microchannel designs. However, flow in the heat sinks with C-type and Z-type inlet–outlet configurations is highly asymmetrical in the header regions due to the abrupt diversion of the fluid away from the inlet toward the microchannels in the inlet header region and away from the microchannels toward the outlet in the outlet header region. This effect is least pronounced in the Z-type heat sink with the parallel secondary flow because the orientation of the flow through the secondary channels tends to divert the fluid in the positive x -direction. Similarly, the flow separation

in the header regions is the most pronounced in the C-type heat sink with the parallel secondary flow because the secondary flow orientation in this heat sink tends to divert the fluid away from the outlet region.

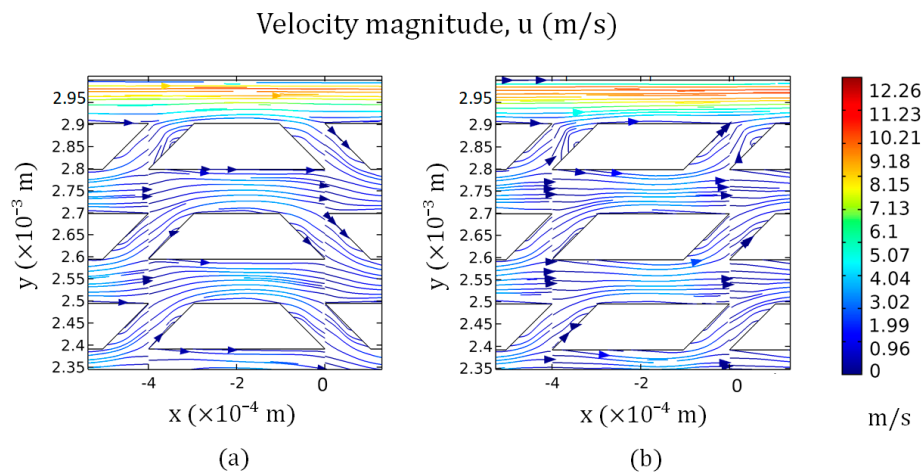


Figure 7. Streamlines over the midplane ($z = 0$) of the heat sink in the vicinity of $x = -2.0 \times 10^{-3}$ m and $y = 2.65 \times 10^{-3}$ m for the Z-type inlet-outlet configuration with (a) regular trapezoidal secondary flow and (b) parallel secondary flow.

Overall, flow separation in the header regions is the highest in the C-type configurations as opposed to the I-type and Z-type configurations, in which the streamlines are relatively symmetrically distributed inside the respective heat sinks. For the C-type configuration, these streamlines are shorter in the mainstream channels nearer to the inlet and outlet and longer in the channels at the further lateral extreme of the heat sink, thereby creating an uneven flow of the circulating fluid in the header regions further away from the inlet and outlet.

Velocity maldistribution factor ω , given by Equation (12), is used to quantify the overall flow separation. This factor is used to characterise the flow distribution over the midplane inside the six resulting configurations of the heat sinks [13].

$$\omega = \frac{u_{\text{std}}}{u_{\text{ave}}} \quad (12)$$

where u_{std} is the standard deviation, and u_{ave} is the average of the velocity magnitude. A lower value of ω over the midplane suggests better flow uniformity inside the fluid domain. The values of ω for the six configurations are summarised in Table 4. For both the regular trapezoidal and parallel secondary flows, the I-type configuration gives the lowest values of ω (0.514 and 0.755, respectively). Considering the lowest flow separation characteristics and the value of ω , the heat sinks with I-type inlet–outlet configuration are used for further study.

Table 4. Values of ω for different inlet–outlet configurations.

Inlet–Outlet Configuration	Velocity Maldistribution Factor, ω	
	Heat Sink A	Heat Sink B
I-type	0.514	0.755
C-type	0.645	0.900
Z-type	0.547	0.996

4.2. Pressure Drop across the Heat Sink

Pressure drop in coolant flow-based heat sinks is primarily due to viscous friction from the walls and obstructions inside the heat sink. The primary purpose of these obstructions is to increase the heat absorption into the coolant through increased surface area and intermixing of flow [11]. However, these obstructions also increase the pressure drop inside the heat sink, thereby increasing the pumping power required for the fluid circulation and thus the operation cost of the heat sink. Therefore, the pressure drop acts as a design constraint in optimising heat sink geometry for maximum thermal absorption with available resources.

The pressure drop across heat sinks A and B and the corresponding rectangular model for the volumetric flow rates of $2.0 \times 10^{-6} \text{ m}^3/\text{s}$ to $4.0 \times 10^{-6} \text{ m}^3/\text{s}$ ranges from $4.0 \times 10^4 \text{ Pa}$ to $1.25 \times 10^5 \text{ Pa}$ for the conventional rectangular heat sink, from $7.0 \times 10^4 \text{ Pa}$ to $2.7 \times 10^5 \text{ Pa}$ for heat sink A, and from $8.0 \times 10^4 \text{ Pa}$ to $3.0 \times 10^5 \text{ Pa}$ for heat sink B, as shown in Figure 8. The pressure drop is higher for heat sinks A and B because it accounts for the additional flow through the secondary channels as well. The phenomena responsible for this increase in pressure drop are two-fold: Firstly, as the fluid enters and exits the secondary flow channels, it impinges onto the walls of the secondary flow passages and the adjacent mainstream channels. This flow behaviour disturbs the hydrodynamic boundary layer, resulting in increased pressure drop in heat sinks A and B. Secondly, flow from the wider regions into the narrower regions inside the flow domain creates a throttling effect in heat sinks A and B, thus contributing to the pressure drop.

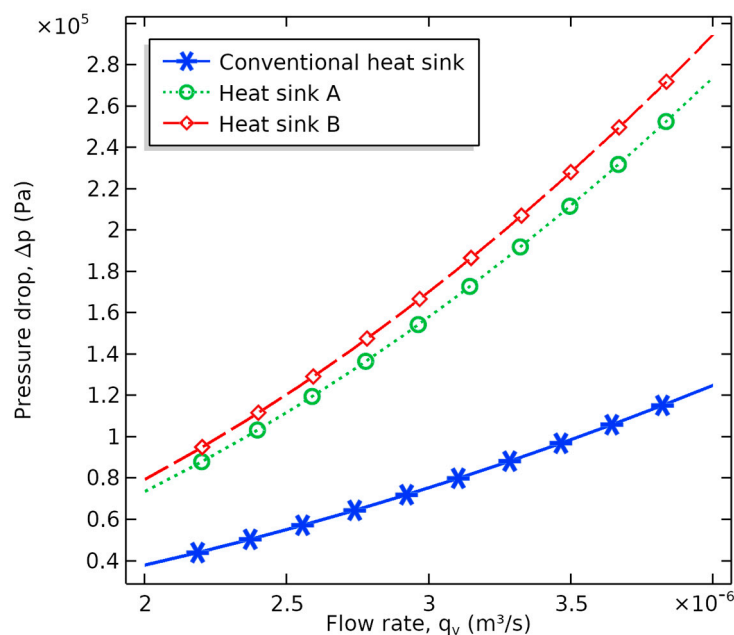


Figure 8. Pressure drop across the heat sinks versus volumetric flow rate.

It is further observed that the pressure drop across the heat sink B is slightly higher than the pressure drop across the heat sink A due to the asymmetric nature of the microchannel design in heat sink B. Nonetheless, the pressure drop across the heat sinks A and B follows approximately the same trajectory because of the same number of secondary flow passages in each heat sink by design. It is also noted that the higher pressure drop in heat sinks with secondary flow channels indicates intensification in the pumping power requirement solely due to the secondary flow channels, which may result in commercial unfeasibility of the considered heat sinks when the operation cost is a major concern for the manufacturer. Finally, the slope of pressure drop increases as the flow rate is increased, thereby suggesting higher operation costs for higher flow rates.

4.3. Temperature Distribution over the Heat Sink

Figure 9 compares the average temperature at the base plate for heat sinks A and B with simulations conducted for the conventional rectangular design for the volumetric flow rates of $2.0 \times 10^{-6} \text{ m}^3/\text{s}$ to $4.0 \times 10^{-6} \text{ m}^3/\text{s}$. A decrease in the average temperature from 309 K to 307.3 K is observed for heat sinks A and B, whereas this decrease is from 310 K to 308.5 K for the conventional rectangular geometry. Among the three designs considered, the geometries with secondary flow exhibit a decrease in the average base plate temperature, which indicates an enhancement in thermal performance. This situation can be attributed firstly to the larger interfacial area for heat transfer. Secondly, flow through the secondary passage disrupts the hydrodynamic boundary layer, which redevelops at the leading edge of the adjacent microchannel wall. This phenomenon leads to a decrease in the thickness of the average thermal boundary layer, thereby resulting in enhanced thermal performance. Moreover, the average base plate temperature for heat sinks A and B assumes nearly equal values for all flow rates because of the same number of secondary flow passages in each heat sink.

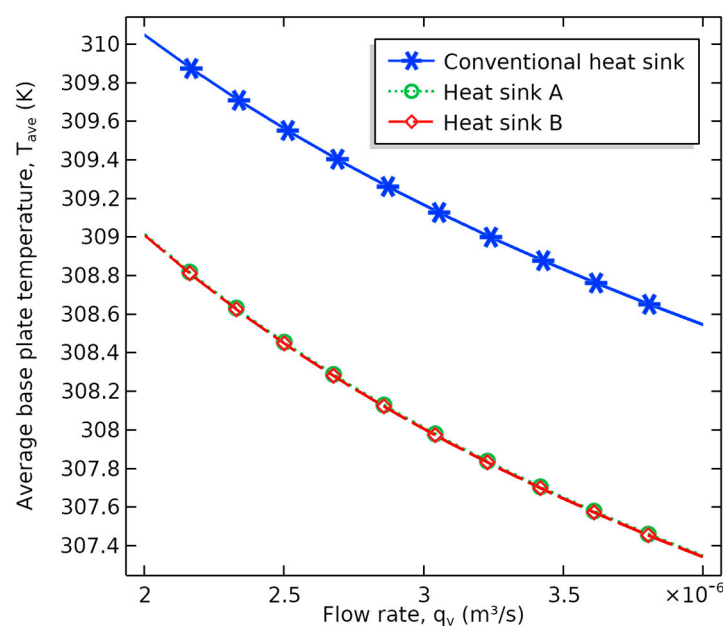


Figure 9. Average temperature at the base plate of the heat sink versus volumetric flow rate.

The intensity of hotspots at the base plate of the heat sinks is evaluated in Figure 10, which plots the maximum base plate temperature for the volumetric flow rates of $2.0 \times 10^{-6} \text{ m}^3/\text{s}$ to $4.0 \times 10^{-6} \text{ m}^3/\text{s}$ for the conventional model and the heat sinks A and B. The conventional model and the heat sink A exhibit the lowest maximum base plate temperature range (from 314.3 K to 310.7 K) among the three models. This temperature ranges higher (from 314.7 K to 311.2 K) for the heat sink B because of the relative asymmetry in its microchannel geometry (parallel secondary flow passages) directing the fluid in the positive y-direction as the fluid flows through the microchannels. Figure 10 further indicates a rapid decrease in the intensity of hotspots for higher volumetric flow rates, thereby suggesting the possible commercial viability of the heat sink design at higher flow rates.

The hotspots are depicted in further detail in Figure 11, which plots the base plate temperature for the volumetric flow rate of $4.0 \times 10^{-6} \text{ m}^3/\text{s}$ for the three microchannel heat sink designs. The hotspots are more pronounced near the leading edge of the base plate in each heat sink due to relatively lesser absorption of heat by the coolant from these regions which is due to heat absorption in the preceding region of the flow channel. Figure 11 further shows that the low-temperature region over the base plate is considerably higher in the vicinity of the inlet header regions in comparison with other regions in all three heat sink designs. This profile of temperature can be attributed to the flow impingement onto the bottom surface in this region as the fluid normally enters the heat sink. Further, in the positive

x-direction, the temperature profile on the base plate in the vicinity of the microchannels is higher at the lateral extreme compared with the region near the x -axis. This situation can be explained by the longer trajectory required for the fluid to reach the lateral extreme of the microchannels in case of the conventional rectangular model, thereby decreasing the capacity of the flow to absorb heat in these regions. The longer trajectory additionally serves to decrease the flow velocity, which further decreases the heat transfer in these regions. This decreased heat transfer is more pronounced in the conventional heat sink because of the absence of the secondary flow passages, which facilitate shorter fluid trajectory into the lateral extremes of the microchannels as compared with heat sinks A and B, which present a uniform temperature profile on the base plate in the vicinity of the microchannels.

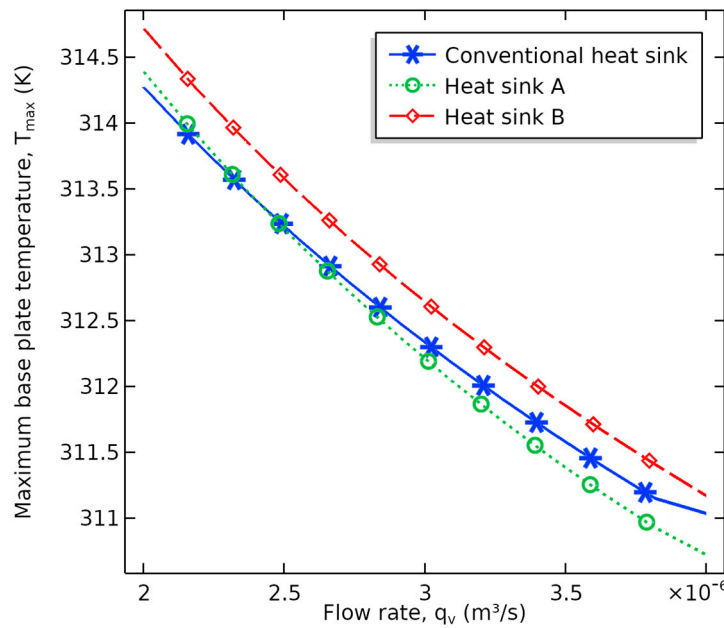


Figure 10. Maximum temperature at the base plate of the heat sink versus volumetric flow rate.

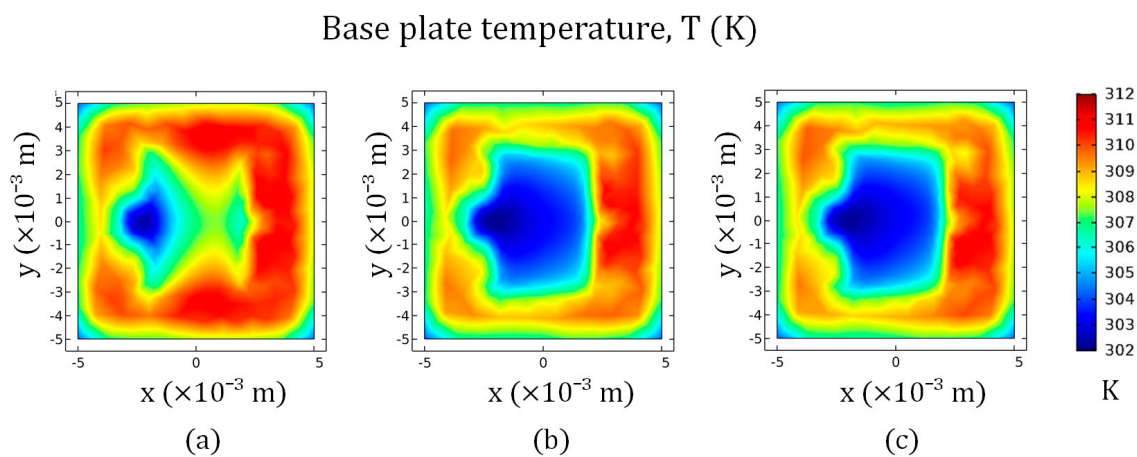


Figure 11. Temperature contour plot at the base plate of the heat sink at the volumetric flow rate of $4.0 \times 10^{-6} \text{ m}^3/\text{s}$ for the (a) I-type conventional flow, (b) I-type regular trapezoidal secondary flow (heat sink A), and (c) I-type parallel secondary flow (heat sink B).

4.4. Hydraulic Characteristics inside the Secondary Flow Channel

In each heat sink design with secondary flow passages, stagnation points can be observed in some secondary flow passages using the pressure contour plots. Figure 12 shows stagnation points formed by plotting pressure contours over $z = 0$ in the vicinity of $x = 1.2 \times 10^{-3} \text{ m}$ and $y = 8.2 \times 10^{-4} \text{ m}$ for

the heat sink A and in the vicinity of $x = 8.0 \times 10^{-4}$ m and $y = -2.44 \times 10^{-3}$ m for the heat sink B. The formation of stagnation points suggests the existence of a pair of counter-rotating vortices, with one vortex at each end of the secondary flow channels [12].

Pressure, p (Pa)

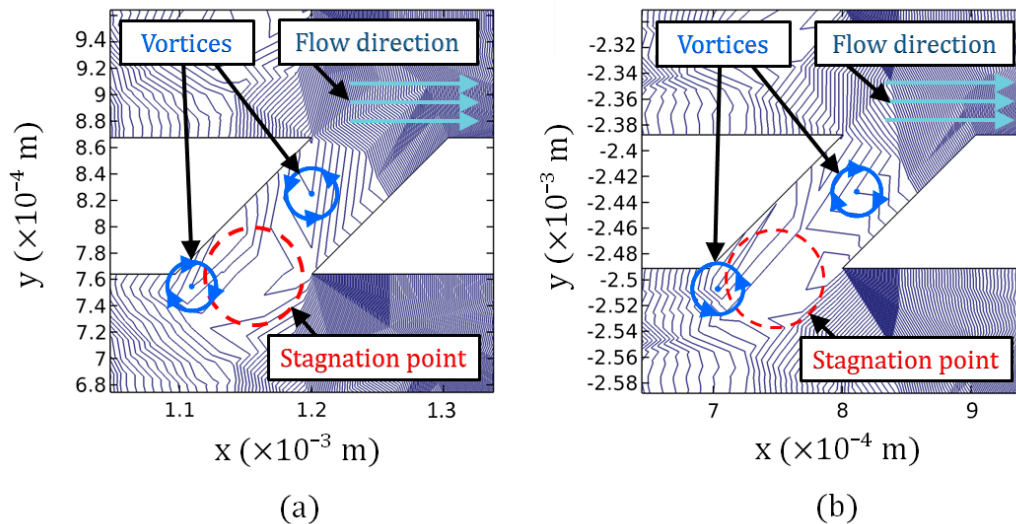


Figure 12. Close-up view of pressure contours over midplane ($z = 0$) of the heat sinks (a) in the vicinity of $x = 1.20 \times 10^{-3}$ m and $y = 8.20 \times 10^{-4}$ m for the heat sink A (regular trapezoidal secondary flow) and (b) in the vicinity of $x = 8.0 \times 10^{-4}$ m and $y = -2.44 \times 10^{-3}$ m for the heat sink B (parallel secondary flow).

Vortices can be generated in a fluid flow that experiences interruptions. In the present case, the flow in each mainstream channel is being diverted into the adjacent mainstream channels, thereby creating flow interruptions inside the secondary flow channels. Hence, upper vortices are created by the fluid diversion from the upper mainstream channel into the lower mainstream channel ($-y$ -direction). Similarly, the lower vortices are created when the flow is diverted from a lower mainstream channel into an upper mainstream channel ($+y$ direction).

Thus, the creation of stagnation points inside the grooves can be explained as follows: a counter-rotating pair of vortices causes the fluid to flow in three directions simultaneously. In the case of the trapezoidal secondary flow, the first direction of flow is from the upper vortex into the lower vortex and the lower mainstream channel ($-y$ direction), the second direction is from the upper vortex into the upper mainstream channel ($+x$ direction), and the third direction is from the lower vortex into the upper mainstream channel ($+y$ direction), creating a stagnation point inside the groove, as shown in Figure 12a. Similarly, in case of the parallel secondary flow, the stagnation point is generated as shown in Figure 12b, where the first direction of flow is from the lower vortex into the upper vortex and the upper mainstream channel ($+y$ direction), the second direction is from the lower vortex into the lower mainstream ($+x$ direction), and the third direction is from the upper vortex into the lower mainstream channel ($-y$ direction). A component of temperature decrease in the microchannels with the secondary flow can be attributed to the mixing of fluid created by these vortices.

5. Conclusions

The thermal performance of two different microchannel designs with secondary flow passages was investigated in this study. One design had secondary flow passages with a regular trapezoidal orientation, and the other design had secondary flow passages with a parallel orientation. These designs were tested against the I-type, C-type, and Z-type inlet–outlet configurations. The results were computed

in terms of velocity and pressure profiles inside the flow domain and temperature on the base plate of the heat sink. The findings of the study can be concluded as follows:

- Better flow velocity uniformity is obtained for the I-type inlet-outlet configuration than for the C-type and Z-type configurations. The lowest velocity maldistribution factor suggested optimal flow distribution for the I-type configuration for each of the two microchannel designs considered. Further investigation of the thermal performance was therefore conducted using the I-type inlet–outlet configuration.
- For designs with secondary flow passages, the pressure drop rapidly increased as the volumetric flow rate increased due to the impinging and throttling effects associated with the secondary flow channels.
- The heat sink designs with secondary flow exhibit enhanced heat absorption and temperature uniformity over the base plate especially at higher flow rates. This enhancement in thermal absorption can be attributed to the increased interfacial area coupled with a decrease in the average thickness of the thermal boundary layer and the formation of vortices due to disruption in the hydrodynamic boundary layer.
- Virtually the same performance increase is observed in both regular trapezoidal and parallel orientations of the secondary flow passages considered indicating primary dependence of the thermal enhancement on the increase in the wetted area as a result of the grooves.
- Overall, heat sinks with secondary flow passages in the regular trapezoidal orientation exhibit enhanced thermal performance with reduced risk of thermal expansion for the microelectronic components mounted at the base plate.

Author Contributions: Conceptualization, S.A.M. and C.W.P.; methodology, S.A.M. and C.W.P.; software, S.A.M. and C.W.P.; validation, S.A.M., T.A.C. and C.W.P.; formal analysis, S.A.M. and T.A.C.; investigation, S.A.M., T.A.C. and C.W.P.; resources, T.A.C., G.M.K. and C.W.P.; data curation, S.A.M., T.A.C. and C.W.P.; writing—original draft preparation, S.A.M., T.A.C. and C.W.P.; writing—review and editing, S.A.M., T.A.C., G.M.K. and C.W.P.; visualization, S.A.M., T.A.C. and C.W.P.; supervision, G.M.K. and C.W.P.; project administration, G.M.K. and C.W.P.; funding acquisition, C.W.P. All authors have read and agreed to the published version of the manuscript.

Funding: This study is supported by the National Research Foundation of Korea and funded by the Korean government (MSIP Grant No. 2020R1A2B5B02002512, 2020R1A4A1018652).

Conflicts of Interest: The authors declare no conflict of interest. The funders had no role in the design of the study; in the collection, analyses, or interpretation of data; in the writing of the manuscript, or in the decision to publish the results.

Nomenclature

c	specific heat capacity at constant pressure [$\text{J kg}^{-1} \text{K}^{-1}$]
D	diameter [m]
D_h	hydraulic diameter [m]
H	height [m]
k	thermal conductivity [$\text{W m}^{-1} \text{K}^{-1}$]
L	length [m]
n_{ch}	number of microchannels
p	pressure [Pa]
q_v	volumetric flow rate [$\text{m}^3 \text{s}^{-1}$]
q_w	heat flux [W m^{-2}]
s	width primary flow channel [m]
t	thickness of microchannel wall [m]
T	temperature [K]
u	velocity magnitude [m s^{-1}]
α	maximum wall separation between adjacent groove (fluid region) [m]
β	maximum wall separation between adjacent grooves (solid region) [m]

θ	angle of secondary flow passage relative to $-x$ -axis
μ	dynamic viscosity [Pa s]
ρ	density [kg m^{-3}]
ω	velocity mal-distribution factor

Subscripts

ave	average
f	fluid
in	inlet
max	maximum
out	outlet
p	secondary flow in parallel orientation
s	solid
std	standard deviation
t	secondary flow in regular trapezoidal orientation

References

1. Tuckerman, D.B.; Pease, R.F.W. High-Performance Heat Sinking for VLSI. *IEEE Electron Device Lett.* **1981**, *2*, 126–129. [[CrossRef](#)]
2. Xing, K.Q.; Tao, Y.X.; Hao, Y.L. Performance evaluation of liquid flow with PCM particles in Microchannels. *J. Heat Transf.* **2005**, *127*, 931–940. [[CrossRef](#)]
3. Li, Y.; Xia, G.; Jia, Y.; Ma, D.; Cai, B.; Wang, J. Effect of geometric configuration on the laminar flow and heat transfer in microchannel heat sinks with cavities and fins. *Numer. Heat Transf. Part A Appl.* **2017**, *71*, 528–546. [[CrossRef](#)]
4. Chai, L.; Wang, L. Thermal-hydraulic performance of interrupted microchannel heat sinks with different rib geometries in transverse microchambers. *Int. J. Therm. Sci.* **2018**, *127*, 201–212. [[CrossRef](#)]
5. Abdollahi, A.; Sharma, R.N.; Mohammed, H.A.; Vatani, A. Heat transfer and flow analysis of Al₂O₃-Water nanofluids in interrupted microchannel heat sink with ellipse and diamond ribs in the transverse microchambers. *Heat Transf. Eng.* **2018**, *39*, 1461–1469. [[CrossRef](#)]
6. Reyes, M.; Arias, J.R.; Velazquez, A.; Vega, J.M. Experimental study of heat transfer and pressure drop in micro-channel based heat sinks with tip clearance. *Appl. Therm. Eng.* **2011**, *31*, 887–893. [[CrossRef](#)]
7. Hung, T.C.; Sheu, T.S.; Yan, W.M. Optimal thermal design of microchannel heat sinks with different geometric configurations. *Int. Commun. Heat Mass Transf.* **2012**, *39*, 1572–1577. [[CrossRef](#)]
8. Hung, T.C.; Yan, W.M. Optimization of a microchannel heat sink with varying channel heights and widths. *Numer. Heat Transf. Part A Appl.* **2012**, *62*, 722–741. [[CrossRef](#)]
9. Arani, A.A.A.; Akbari, O.A.; Safaei, M.R.; Marzban, A.; Alrashed, A.A.A.A.; Ahmadi, G.R.; Nguyen, T.K. Heat transfer improvement of water/single-wall carbon nanotubes (SWCNT) nanofluid in a novel design of a truncated double-layered microchannel heat sink. *Int. J. Heat Mass Transf.* **2017**, *113*, 780–795. [[CrossRef](#)]
10. Tao, W.Q.; He, Y.L.; Wang, Q.W.; Qu, Z.G.; Song, F.Q. A unified analysis on enhancing single phase convective heat transfer with field synergy principle. *Int. J. Heat Mass Transf.* **2002**, *45*, 4871–4879. [[CrossRef](#)]
11. Steinke, M.E.; Kandlikar, S.G. Single-phase heat transfer enhancement techniques in microchannel and minichannel flows. *Proc. Second Int. Conf. Microchannels Minichannels* **2004**, 141–148. [[CrossRef](#)]
12. Raja Kuppasamy, N.; Saidur, R.; Ghazali, N.N.N.; Mohammed, H.A. Numerical study of thermal enhancement in micro channel heat sink with secondary flow. *Int. J. Heat Mass Transf.* **2014**, *78*, 216–223. [[CrossRef](#)]
13. Lu, M.C.; Wang, C.C. Effect of the inlet location on the performance of parallel-channel cold-plate. *IEEE Trans. Compon. Packag. Technol.* **2006**, *29*, 30–38. [[CrossRef](#)]
14. Brinda, R.; Joseph Daniel, R.; Sumangala, K. Ladder shape micro channels employed high performance micro cooling system for ULSI. *Int. J. Heat Mass Transf.* **2012**, *55*, 3400–3411. [[CrossRef](#)]
15. Leela Vinodhan, V.; Rajan, K.S. Computational analysis of new microchannel heat sink configurations. *Energy Convers. Manag.* **2014**, *86*, 595–604. [[CrossRef](#)]
16. Mohib Ur Rehman, M.; Cheema, T.A.; Khan, M.; Abbas, A.; Ali, H.; Park, C.W. Parametric evaluation of a hydrofoil-shaped sidewall rib-employed microchannel heat sink with and without nano-encapsulated phase change material slurry as coolant. *Appl. Therm. Eng.* **2020**, *178*, 115514. [[CrossRef](#)]

17. Ahmad, F.; Cheema, T.; Ur Rehman, M.M.; Ilyas, M.; Park, C.W. Thermodynamic Analysis of Microchannel Heat Sink with Cylindrical Ribs and Cavities. *J. Heat Transf.* **2020**, *142*, 1–11. [[CrossRef](#)]
18. Xia, G.D.; Jiang, J.; Wang, J.; Zhai, Y.L.; Ma, D.D. Effects of different geometric structures on fluid flow and heat transfer performance in microchannel heat sinks. *Int. J. Heat Mass Transf.* **2015**, *80*, 439–447. [[CrossRef](#)]
19. Koo, J.; Kleinstreuer, C. Viscous dissipation effects in microtubes and microchannels. *Int. J. Heat Mass Transf.* **2004**, *47*, 3159–3169. [[CrossRef](#)]
20. Cole, K.D.; Çetin, B. The effect of axial conduction on heat transfer in a liquid microchannel flow. *Int. J. Heat Mass Transf.* **2011**, *54*, 2542–2549. [[CrossRef](#)]

Publisher's Note: MDPI stays neutral with regard to jurisdictional claims in published maps and institutional affiliations.



© 2020 by the authors. Licensee MDPI, Basel, Switzerland. This article is an open access article distributed under the terms and conditions of the Creative Commons Attribution (CC BY) license (<http://creativecommons.org/licenses/by/4.0/>).